



1 Near-threshold aeolian sand transport: Effects of 2 boundary layer flow conditions

3 Ting Jin¹, Lifeng Zhou²

4 ¹ School of Metallurgical and Energy Engineering, Kunming University of Science and Technology,
5 Kunming, 650000, China

6 ² Yunnan Key Laboratory of Efficient Utilization and Intelligent Control of Agricultural Water
7 Resources, Kunming University of Science and Technology, Kunming, 650000, China

8 *Corresponding to:* Lifeng Zhou (zhoulf@kust.edu.cn)

9 10 Abstract

11 Boundary layer thickness is a critical factor in aeolian sand transport, as it governs the scale of
12 energy-containing turbulent structures, yet its specific mechanisms remain inadequately quantified.
13 Previous studies have established the role of turbulence in particle entrainment but often overlook
14 systematic variations in boundary layer thickness. This study aims to clarify how boundary layer
15 thickness modulates wall-shear stress fluctuations, threshold wind velocities, sand flux, and particle
16 kinematics. We use the three-dimensional large-eddy simulation coupled with a saltation model to
17 investigate these interactions. Results reveal that increased boundary layer thickness enhances
18 extreme-value probability density of wall-shear stress and significantly lowers impact entrainment
19 and rebound thresholds—the latter dropping to less than 50% of conventional wind-tunnel values.
20 Sand transport response is velocity-dependent: at low velocities, transport rises markedly with
21 thickness under fluid-driven entrainment; the effect diminishes at moderate velocities; and at high
22 velocities, transport scales proportionally with thickness under splash-dominated entrainment.
23 Moreover, thicker boundary layers intensify near-bed particle activity, elevating particle velocities
24 and concentrations, reducing intermittency, increasing saltation height, and enlarging mean and
25 variance of airborne particle diameters. These findings elucidate how boundary layer thickness
26 modulates aeolian sand transport via turbulence–particle interactions, offering key insights for
27 improving atmospheric and climate models and advancing the physics of turbulence-driven
28 sediment transport in atmospheric boundary layer.

29 **Keywords:** Boundary layer thickness; Aeolian sand transport; Turbulent structures; Threshold wind
30 velocity; Atmospheric boundary layer

31
32



33 1. Introduction

34 Wind-driven soil particle movement, also known as aeolian transport, is a key geological and
 35 climatic process in arid and desert regions (Shao, 2008). Near-threshold aeolian sand transport
 36 occurs around the threshold wind velocity and is characterized by intermittent bursts of intense
 37 activity separated by quiescent periods (Stout and Zobeck, 1997; Leenders et al., 2005; Carneiro et
 38 al., 2015; Martin and Kok, 2018). Driven by natural wind, this highly unstable process significantly
 39 contributes to total mass flux and plays a crucial role in dune evolution, soil erosion, and dust
 40 emission. However, its quantitative prediction remains challenging (Martin and Kok, 2018) due to
 41 the multiscale nature of turbulent wind fluctuations (Butterfield, 1998; Mathis et al., 2009; Huang
 42 et al., 2020; Zhang et al., 2022) and the path-dependent response of sediment transport to these
 43 fluctuations (Kok, 2010a).

44 Accurate prediction of transport rate and intensity is essential for understanding the formation
 45 and evolution of aeolian landforms (Sherman et al., 1998). Modeling efforts have combined
 46 theoretical, experimental, and numerical approaches. Early theoretical models, such as Kawamura
 47 (1951), incorporated a critical shear velocity for particle entrainment (the fluid threshold,
 48 $u_*' = A[g d_p (\rho_p - \rho) / \rho]^{1/2}$, where d_p is particle diameter, ρ_p and ρ are particle and air
 49 densities, respectively), and proposed a cubic relationship between transport rate and friction
 50 velocity above this threshold, following Bagnold (1941) formulation (coefficient $A = 0.1$). Kok
 51 (2010b) later extended White's (1979) model by introducing a probabilistic framework. Wind tunnel
 52 experiments have been equally influential: Zhou et al. (2002) tested the Bagnold ($u_* \geq 0.47 \text{ m} \cdot \text{s}^{-1}$,
 53 u_* is friction velocity) and Kawamura ($u_*' \leq u_* < 0.35 \text{ m} \cdot \text{s}^{-1}$) equations under different wind
 54 velocities and highlighted the central role of threshold velocity. Dong et al. (2003) showed that the
 55 threshold coefficient (A) decreases linearly with particle Reynolds number. Creyssels et al. (2009)
 56 observed a quadratic, rather than cubic, dependence of transport on friction velocity near the
 57 threshold, consistent with numerical simulations by Almeida et al. (2006) using Reynolds-averaged
 58 methods (critical shear velocity = $0.35 \text{ m} \cdot \text{s}^{-1}$).

59 Despite these advances, most models assume steady, continuous sediment transport governed
 60 by a single fluid threshold. They fail to capture near-threshold behavior where other critical
 61 velocities, such as the impact entrainment threshold (for sustaining continuous transport) and the
 62 rebound threshold (for compensating energy loss from particle bouncing), are important. Predictions
 63 under such conditions are therefore often inaccurate.

64 Near-threshold transport is highly intermittent and distinct from steady-state conditions
 65 (Rasmussen and Sørensen, 1999). It is strongly influenced by interactions between turbulent
 66 coherent structures and sand particles, with different turbulent scales acting through different



67 mechanisms (Liu et al., 2021). Boundary layer thickness is a key parameter that shapes near-wall
 68 turbulence by influencing the Reynolds number, extent of the logarithmic layer, behavior of large-
 69 scale structures, and distribution of turbulent energy production (Marusic et al., 2017). In wind
 70 tunnels, the boundary layer thickness typically ranges from $0.1 \sim 0.2 \text{ m}$ (Clifton et al., 2006;
 71 Parajuli et al., 2016; Li et al., 2020), whereas in the natural atmosphere, it can reach $100 \sim 200 \text{ m}$
 72 (Wang and Zheng, 2016). Consequently, even at identical friction velocities, friction Reynolds
 73 numbers may differ by orders of magnitude, leading to marked differences in transport behavior.

74 Field studies have shown that sediment transport often occurs below the entrainment threshold
 75 in wind tunnels (Rasmussen and Sørensen, 1999), characterized by strong spatiotemporal variability
 76 (Stout and Zobeck, 1997; Baas and Sherman, 2006; Ellis et al., 2012; Huang et al., 2020).
 77 Temporally, intermittent events in the field persist for much longer (Sherman et al., 2013) than in
 78 wind tunnels (Wang et al., 2014). Spatially, transport commonly appears as streamers linked to
 79 large-scale turbulent structures generated higher in the boundary layer (Baas and Sherman, 2005;
 80 Sherman et al., 2013). Streamers in the field can be tens of times longer than those in wind tunnel
 81 experiments (Sherman et al., 2013). Pähtz et al. (2018) emphasized that boundary layer thickness
 82 and turbulent structures are as important as mean shear stress and particle properties in determining
 83 sediment initiation. As a result, conventional incipient motion models—calibrated in wind tunnels—
 84 tend to overestimate the wind velocities required for natural transport. This discrepancy is also
 85 crucial for predicting aeolian activity on extraterrestrial surfaces, such as Mars and Titan, where
 86 boundary layer effects must be considered.

87 While previous studies have highlighted the importance of turbulent fluctuations, most have
 88 focused on the velocity variability rather than explicitly resolving turbulent structures. For example,
 89 Spies et al. (2000) and Wang and Zheng (2014) introduced periodic velocity fluctuations into steady
 90 winds and observed enhanced transport at low velocities. Kok and Renno (2009) added turbulence
 91 to logarithmic profiles and found that it altered the trajectories of small saltating particles
 92 ($d_p < 250 \text{ }\mu\text{m}$). Huang et al. (2020) further demonstrated the role of unsteady winds in aeolian
 93 transport. However, such studies did not reproduce realistic turbulent structures and capture their
 94 direct influence on particle motion. Dupont et al. (2013) numerically resolved turbulent structures
 95 and reproduced near-surface aeolian streamers, while Wang et al. (2019) showed that streamers form
 96 mainly in the near-wall regions of large-scale structures. More recently, Feng and Wang (2023)
 97 compared transport statistics across boundary layers of different thicknesses, offering insights into
 98 wind tunnel–field discrepancies, though their simulations used friction velocities
 99 ($0.43 < u_* < 1.19 \text{ m}\cdot\text{s}^{-1}$) well above the fluid threshold ($u_*' = 0.21 \text{ m}\cdot\text{s}^{-1}$). Jin et al. (2024)
 100 investigated near-threshold transport and identified distinct entrainment mechanisms for rebound



101 and impact thresholds, showing that particle energy variability influences transport patterns.
 102 Nonetheless, the role of boundary layer thickness in near-threshold aeolian sand transport remains
 103 poorly understood.

104 To address this gap, the present study builds upon the work of Jin et al. (2024) using three-
 105 dimensional large-eddy simulations coupled with a saltation model. We systematically examine how
 106 boundary layer flow conditions influence both the flow field and near-threshold sediment transport.
 107 Section 2 presents the governing equations, numerical methods, and simulation setup. Section 3
 108 reports the simulation results and analyzes the role of boundary layer thickness. The main findings
 109 are summarized in Section 4.

111 2. Numerical Simulation Approach

112 The fluid in the boundary layer is assumed incompressible and without thermal exchange. The
 113 dimensionless governing equations are the filtered Navier–Stokes equations:

$$\frac{\partial u_i}{\partial x_i} = 0, \quad \frac{\partial u_i}{\partial t} + u_j \frac{\partial u_i}{\partial x_j} = -\frac{\partial p^*}{\partial x_i} + \nu \frac{\partial^2 u_i}{\partial x_j \partial x_j} + \frac{\partial \tau_{ij}}{\partial x_j} + f_i, \quad (1)$$

114 where $i=1,2,3$ denote streamwise, vertical, and spanwise directions, respectively, u_i is the
 115 filtered velocity, t is time, p^* is filtered kinematic pressure, ν is kinematic viscosity, τ_{ij} is
 116 sub-grid scale (SGS) stress, and $f_i = -1/(\Delta_x \cdot \Delta_y \cdot \Delta_z) \sum_{n=1}^{N_p} f_{Di}$ is the volume force exerted by
 117 particles, where $\Delta_x \cdot \Delta_y \cdot \Delta_z$ is grid volume, N_p is the total number of particles within the grid,
 118 and f_{Di} is the drag force.

119 Spatial discretization uses a second-order centered finite-difference scheme with a staggered
 120 grid in the vertical direction. Time integration applies a second-order Crank–Nicholson method.
 121 Further implementation details are available in Kim et al. (2002) and Zheng et al. (2020). The
 122 turbulent flow field is initiated by adding random perturbations to the mean laminar wind velocity
 123 profile. Periodic boundary conditions are imposed horizontally, with a stress-free condition at the
 124 top of the domain. At the bottom boundary, the integral wall model proposed by Yang et al. (2015)
 125 is employed due to its superior performance compared to other approaches (Jin et al., 2023). Sub-
 126 grid scale stress is represented using the scale-dependent dynamic model (Porté-Agel et al., 2000),
 127 consistent with Feng and Wang (2023) and Jin et al. (2024).

128 Particle trajectories are resolved individually in a Lagrangian framework. Particle velocity u_{pi}
 129 is given by:

$$m_p \frac{du_{pi}}{dt} = f_{Di} + m_p g \delta_{i2} = \frac{1}{2} C_{dp} A_p |u(x_p) - u_p| (u_i(x_{pi}) - u_{pi}) + m_p g \delta_{i2} \quad (2)$$

130 where m_p is particle mass, $C_{dp} = 24(1 + 0.15 Re_p^{0.687}) / Re_p$ is the drag coefficient (Clift et al.,



1978), $A_p = \pi d_p^2 / 4$ is the cross-sectional area of the particle, $Re_p = |u(x_p) - u_p| \cdot d_p / \nu$ is the particle Reynolds number, and $u(x_p)$ is the fluid velocity at the particle location interpolated with a third-order Lagrange scheme.

Aerodynamic entrainment is calculated using the residual shear stress rules (Anderson and Haff, 1991; Shao and Li, 1999; Dun and Huang, 2020): $N_a = (m_p \alpha_x u_t)^{-1} (\tau - \tau_t)$, where τ is the local resolved shear stress, τ_t is the threshold of aerodynamic entrainment (fluid threshold), u_t is the friction velocity of sand-free flow, and α_x is an empirical coefficient. Liftoff velocity and angle distributions follow Jin et al. (2024), consistent with the numerical experiments of Jia and Wang (2021). In addition, a splash function is applied when particles impact the surface, accounting for both the rebound of incident particles and the ejection of bed particles (Anderson and Haff, 1991; Dupont et al., 2013). The rebound probability, as well as the velocity and angle distributions of rebounding particles, together with the number, velocity, and angular distributions of newly ejected particles, follow the model of Zheng et al. (2020). Bed particles are initially entrained into the boundary layer by fluid forces, after which the splash mechanism sustains the development of sand transport. To maintain periodicity, particles exiting the computational domain horizontally are reintroduced from the opposite boundary, while those escaping from the top boundary are re-injected into the flow with their vertical velocity reversed.

To examine the effect of boundary layer thickness (δ) on near-threshold transport, two cases were simulated with $\delta = 5.0$ m and 10.0 m. Results from a smaller domain ($\delta = 1.0$ m) partly draw on Jin et al. (2024). The computational domain dimensions are $8\pi\delta \times \delta \times 2\pi\delta$. Grids are uniform in the horizontal direction and stretched vertically using a hyperbolic tangent function with refinement near the wall ($y_1 = 0.012, 0.014$ m for $\delta = 5.0$ m and 10.0 m). For particle field post-processing, identical vertical grid resolution was applied to ensure comparability.

Bed particles follow a slightly skewed Gaussian size distribution with a mean diameter of 200 μm (Zhu et al., 2019; Liu et al., 2022). Particle and air densities are $\rho_p = 2650$ $\text{kg} \cdot \text{m}^{-3}$ and $\rho = 1.2$ $\text{kg} \cdot \text{m}^{-3}$, giving a density ratio of 2208. The α_x and τ_t values are consistent with Jin et al. (2024). Table 1 lists the simulation cases and key parameters.

Table 1. Bulk fluid velocity (u_b), saltation friction velocity (u_*), Shields number ($\theta_* = u_*^2 / [(\rho_p / \rho - 1)gd_p]$), boundary layer thickness (δ), grid sizes in three directions ($N_x \times N_y \times N_z$), and sand transport rate (Q) for 16 simulated cases with sediment transport.

Cases	u_b ($\text{m} \cdot \text{s}^{-1}$)	u_* ($\text{m} \cdot \text{s}^{-1}$)	θ_*	δ (m)	$N_x \times N_y \times N_z$	Q ($\text{kg} \cdot \text{m}^{-1} \cdot \text{s}^{-1}$)
1	2.90	0.10	0.0024	5.0	$512 \times 64 \times 128$	4.65×10^{-7}
2	3.20	0.11	0.0028	5.0	$512 \times 64 \times 128$	4.36×10^{-6}

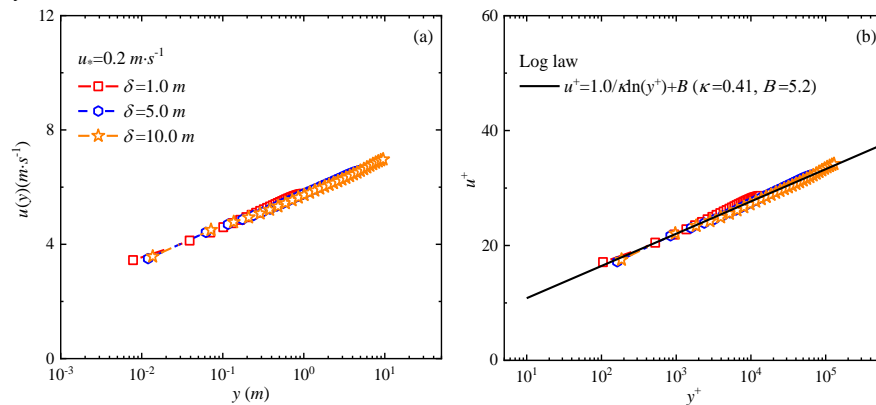


3	3.40	0.12	0.0032	5.0	512×64×128	1.39×10 ⁻⁵
4	4.04	0.14	0.0043	5.0	512×64×128	2.09×10 ⁻⁴
5	5.30	0.18	0.0072	5.0	512×64×128	1.59×10 ⁻³
6	7.70	0.27	0.0168	5.0	512×64×128	8.69×10 ⁻³
7	10.30	0.38	0.0339	5.0	512×64×128	2.41×10 ⁻²
8	2.81	0.09	0.0018	10.0	768×64×192	2.69×10 ⁻⁷
9	3.00	0.10	0.0021	10.0	768×64×192	1.29×10 ⁻⁶
10	3.40	0.11	0.0026	10.0	768×64×192	1.91×10 ⁻⁵
11	3.70	0.12	0.0032	10.0	768×64×192	7.17×10 ⁻⁵
12	4.55	0.14	0.0043	10.0	768×64×192	3.71×10 ⁻⁴
13	6.45	0.20	0.0088	10.0	768×64×192	2.99×10 ⁻³
14	7.00	0.22	0.0106	10.0	768×64×192	4.22×10 ⁻³
15	8.15	0.25	0.0150	10.0	768×64×192	7.28×10 ⁻³
16	10.90	0.36	0.0291	10.0	768×64×192	1.80×10 ⁻²

162

163 3. Results and Discussion

164 This section examines how boundary layer thickness influences near-threshold sand transport.
 165 The simulations span wind velocities from the rebound threshold up to values exceeding the impact
 166 entrainment threshold. To reduce computational cost, each numerically resolved particle represents
 167 multiple physical particles (Dupont et al., 2013), with the representative ratio ranging from 50 to
 168 2000 depending on boundary layer thickness and friction velocity. The analysis begins with mean
 169 wind velocity profiles and wall-shear stress fluctuations, followed by transport behavior and particle
 170 dynamics.



171

172 Fig. 1. (a) Simulated mean wind velocity profiles for three boundary layer thicknesses ($\delta = 1.0$,

173 5.0 , 10.0 m); (b) inner-scale normalized profiles compared with the logarithmic law ($u_\tau =$

174 $0.21 \text{ m} \cdot \text{s}^{-1}$).

175

176 Fig. 1(a) shows mean wind velocity profiles for three boundary layer thicknesses at a fixed



friction velocity, plotted in log-linear coordinates. Profiles overlap closely, with only minor differences at the first grid point for the smallest boundary layer. Near-wall velocities remain consistent across all cases, confirming that the first-grid-point height has a negligible influence. Normalizing the profiles using inner scales ($u^+ = u / u_\tau$, $y^+ = u_\tau y / \nu$) (Fig. 1(b)) shows excellent agreement with the logarithmic law, validating the simulated mean flow fields across boundary layer thicknesses.

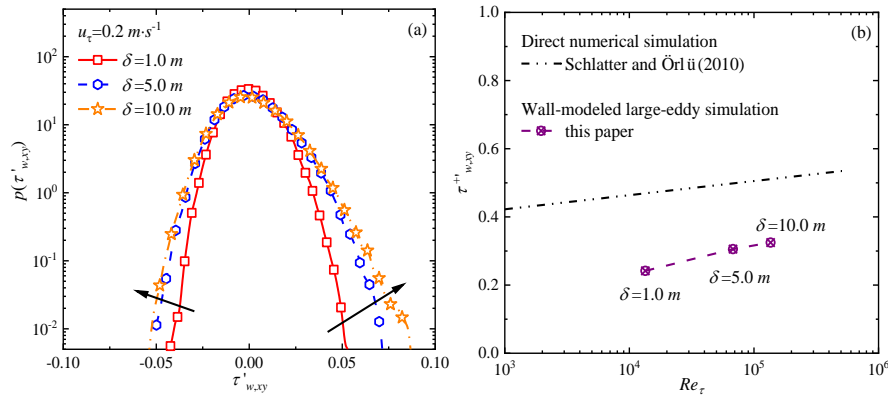


Fig. 2. (a) Probability density distributions and (b) standard deviations of wall-shear stress fluctuations for different boundary layer thicknesses ($\delta = 1.0, 5.0, 10.0$ m).

Particle liftoff is initiated by instantaneous high shear stresses or local pressure imbalances generated by turbulent fluctuations. Boundary layer thickness influences the velocity threshold for entrainment by modulating near-wall turbulent structures and the resulting wall-shear stress field (Lu et al., 2005; Pähitz et al., 2018). Fig. 2(a) shows the probability density distributions of wall-shear stress fluctuations under the same free-stream wind velocity. The simulations reveal clear differences across boundary layer thicknesses. As the boundary layer increases, the probability densities at both tails of the distribution—especially for positive fluctuations above the mean—also increase. This trend arises because the boundary layer thickness constrains the largest turbulent scales (Pähitz et al., 2018). A thicker boundary layer supports a broader range of turbulent scales, producing stronger instantaneous wall-shear stresses. When the boundary layer thickness increases fivefold (from 1.0 m to 5.0 m), the fluctuation amplitude rises markedly, but further increases lead to a slower rate of growth. Fig. 2(b) compares the standard deviation of wall-shear stress fluctuations with the direct numerical simulation results of Schlatter and Örlü (2010). The lower values obtained here reflect the use of wall-modeled large-eddy simulations with relatively coarse grid resolution. Despite this, the Reynolds number dependence across different boundary layer thicknesses is well captured.

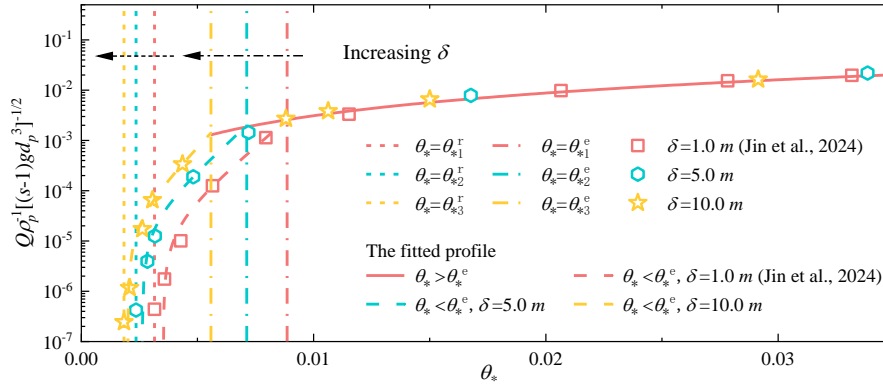


Fig. 3. Simulated sand transport rates under different boundary layer thicknesses ($\delta = 5.0, 10.0 \text{ m}$) and wind velocities.

Large-scale turbulent structures carry significant energy and Reynolds stress (Guala et al., 2006; Balakumar and Adrian, 2007), thereby enhancing energy transfer (Marusic et al., 2010; Serafimovich et al., 2011). The influence of boundary layer thickness on these large structures can further affect particle motion in sand-laden flows. Under simulated conditions with $\delta = 1.0 \text{ m}$, Jin et al. (2024) reported that above the impact entrainment threshold (θ_*^e), the time-averaged sand transport rate scales shear stress raised to the power of 1.5, whereas below θ_*^e , it varies exponentially with shear stress. As shown in Fig. 3, the simulated sand transport rates across different boundary layer thicknesses and dimensionless wind velocities follow the same trend, with fitted curves yielding a high correlation coefficient (R^2). However, the threshold wind velocities depend strongly on the boundary layer thickness. For example, the impact entrainment thresholds required for sustained continuous transport are $\theta_{*2}^e = 0.00712$ and $\theta_{*3}^e = 0.00558$ for $\delta = 5.0 \text{ m}$ and 10.0 m , respectively (dot-dashed lines in Fig. 3). These correspond to impact threshold wind velocities (u_*^e) of 0.18 and $0.16 \text{ m} \cdot \text{s}^{-1}$, equal to 0.58 and 0.52 times the fluid threshold ($u_*^f = 0.31 \text{ m} \cdot \text{s}^{-1}$). Similarly, rebound thresholds were $\theta_{*2}^r = 0.00235$ and $\theta_{*3}^r = 0.00184$ (dashed lines in Fig. 3), corresponding to rebound threshold wind velocities (u_*^r) of 0.1 and $0.09 \text{ m} \cdot \text{s}^{-1}$, or 0.32 and 0.29 times the fluid threshold.

For a particle size of $200 \text{ }\mu\text{m}$, the threshold coefficient in a fluctuating flow field is about 1.5 times that in the time-averaged flow (Li et al., 2020a). Based on the entrainment threshold of $u_*^f = 0.21 \text{ m} \cdot \text{s}^{-1}$ obtained from wind tunnel experiments, the rebound thresholds are 47.6% and 42.9% of this value, respectively. Field studies also indicate that transport may occur when the friction velocity is just 50% of the wind-tunnel threshold (Rasmussen and Sørensen, 1999). Given measurement uncertainties and the difficulty detecting particles close to the bed (Jin et al., 2021),



the thresholds under field conditions may be even lower than those estimated here. Fig. 4(a) further shows that both θ_s^* and θ_s^* decrease with increasing boundary layer thickness, with the decline in θ_s^* more pronounced.

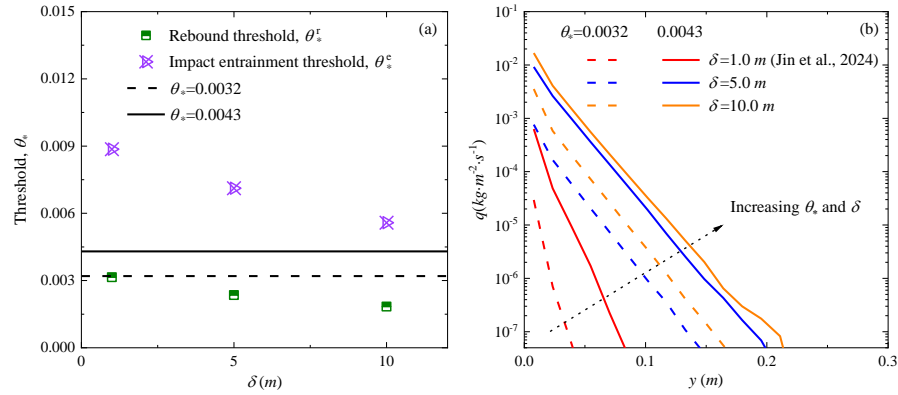


Fig. 4. (a) Rebound and impact entrainment thresholds and (b) sediment transport intensity for different boundary layer thicknesses (Data for $\delta = 1.0$ m taken from Jin et al. (2024)).

Notably, when $\theta_s > \theta_s^*$, the differences in sand transport rates across varying boundary layer thicknesses become negligible. In contrast, when $\theta_s < \theta_s^*$, the sand transport rate scales with the boundary layer thickness and rises sharply with increasing wind velocity (Rasmussen and Sørensen, 1999). For example, at $\theta_s = 0.0043$, the transport rates for $\delta = 5.0$ m and 10.0 m are 19 and 33 times that for $\delta = 1.0$ m, respectively; at $\theta_s = 0.0032$, the corresponding factors increase to 29 and 149, demonstrating that the influence of boundary layer thickness is more pronounced at lower wind velocities. These findings suggest that in real field conditions, sediment transport rates may be higher and threshold wind velocities lower than predicted in conventional wind tunnels. Feng and Wang (2023) reported a similar trend, observing that sediment transport rates increase with boundary layer thickness at wind velocities ($\theta_s > 0.15$, $u_s > 0.8 \text{ m} \cdot \text{s}^{-1}$ in their study) well above the near-threshold regime considered in this study. This implies that the effect of boundary layer thickness on sediment flux depends on the wind velocity and the dominant particle entrainment mechanism.

Specifically, at wind velocities below the impact entrainment threshold (θ_s^*), thicker boundary layers generate higher instantaneous wall-shear stresses, enhancing fluid-driven particle flux and increasing the sand transport rate. When wind velocities far exceed the impact entrainment threshold ($\theta_s > 21 \theta_{s2}^*$ or $> 27 \theta_{s3}^*$ according to Feng and Wang (2023)), splash-driven entrainment dominates, and the sand transport flux becomes approximately proportional to the boundary layer thickness. In the transitional wind velocity regime between these limits, both fluid- and splash-



255 driven processes are relatively insensitive to boundary layer thickness, resulting in minimal
 256 variation in transport rates.

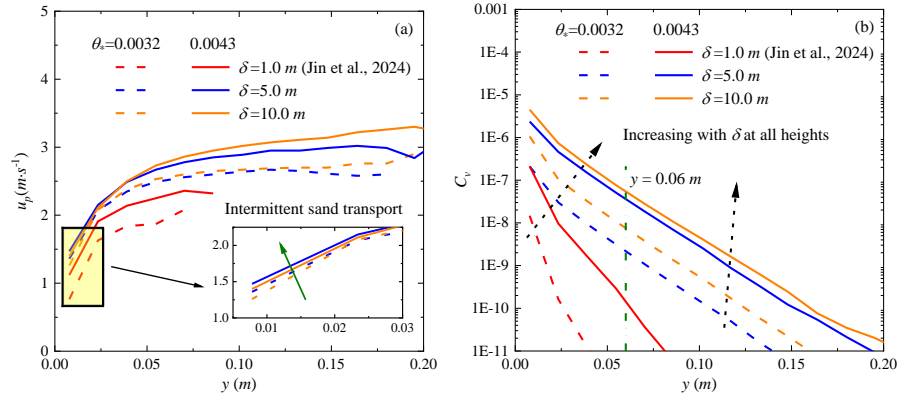
257 Sediment transport intensity, which quantifies the non-uniform vertical distribution of sand
 258 flux, serves as a key metric linking the microscopic mechanisms of aeolian sand movement—such
 259 as particle entrainment and collisions—to macroscopic outcomes, including the overall sediment
 260 transport rate. Using the same grid resolution (grid size of $\delta = 1.0\text{ m}$), Fig. 4(b) shows how
 261 sediment transport intensity varies with height for different boundary layer thicknesses
 262 ($\delta = 5.0, 10.0\text{ m}$) and dimensionless shear velocities ($\theta_* = 0.0032, 0.0043$). For comparison,
 263 simulation results for $\delta = 1.0\text{ m}$ (Jin et al., 2024) are also included to highlight the combined
 264 effects of wind velocity and boundary layer thickness. All profiles exhibit an exponential decay with
 265 increasing height.

266 As illustrated in Fig. 4(a), the selected wind velocities ($\theta_* = 0.0032, 0.0043$) are above the
 267 rebound threshold but below the impact entrainment threshold for all three boundary layer
 268 thicknesses, indicating that sediment transport occurs intermittently under these conditions. As both
 269 wind velocity and boundary layer thickness increase, the sediment transport intensity rises across
 270 all heights, with differences becoming more pronounced at greater heights. The effect of boundary
 271 layer thickness is particularly significant at lower wind velocities. For instance, at a height of
 272 $y = 0.04\text{ m}$, the sediment transport intensity for $\delta = 5.0\text{ m}$ and 10.0 m increases by
 273 approximately 1000 and 3000 times, respectively, relative to $\delta = 1.0\text{ m}$ at $\theta_* = 0.0032$. At
 274 $\theta_* = 0.0043$, the corresponding increases are about 100 and 150 times, indicating that the influence
 275 of boundary layer thickness diminishes as wind velocity increases. Importantly, the variations in
 276 sediment transport intensity due to boundary layer thickness at this height are far larger than those
 277 observed in the total transport rate, since the sediment transport intensity for $\delta = 1.0\text{ m}$ is
 278 relatively low and contributes only minimally to the overall flux.

279 Fig. 5(a) shows the vertical profile of mean horizontal particle velocity. Unlike continuous
 280 transport conditions—where wind velocities exceed the impact entrainment threshold and thicker
 281 boundary layers generally result in faster particle movement at the same wind velocity (Feng and
 282 Wang, 2023)—the relationship under sub-threshold conditions is non-monotonic. At different wind
 283 velocities, particle velocity for $\delta = 1.0\text{ m}$ is lower than for $\delta = 5.0\text{ m}$, but shows little change
 284 when the boundary layer thickness increases further to $\delta = 10.0\text{ m}$. As wind velocity rises, the
 285 velocity difference between $\delta = 1.0\text{ m}$ and $\delta = 5.0\text{ m}$ or 10.0 m diminishes. Simulation
 286 results for $\delta = 5.0\text{ m}$ and 10.0 m also demonstrate that near-wall particle velocity is
 287 proportional to wind velocity (see inset of Fig. 5(a)), confirming that sediment transport remains
 288 intermittent when $\theta_* < 0.0043$ (Jin et al., 2024). However, greater boundary layer thickness



289 reduces this intermittency, leading to smaller velocity variations across different wind velocities
 290 under thicker boundary layers.



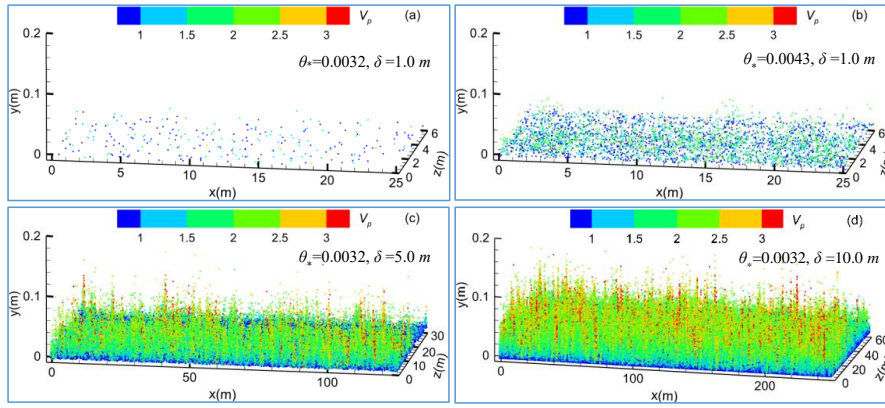
291
 292 Fig. 5. Vertical profiles of (a) mean particle velocity and (b) particle volume fraction for different
 293 boundary layer thicknesses ($\delta = 5.0, 10.0 \text{ m}$).
 294

295 Feng and Wang (2023) observed that particle volume fraction increases with boundary layer
 296 thickness only in regions far from the wall (e.g., $y > 0.06 \text{ m}$ when $\theta_* = 0.0427$). In contrast, the
 297 present results show that under the same wind velocity, particle volume fraction is proportional to
 298 boundary layer thickness across all heights (Fig. 5(b)). This discrepancy arises due to the
 299 predominance of fluid-driven particle entrainment under low wind velocities rather than splash
 300 events. These fluid-driven particles move at lower velocities, and only a small fraction gains
 301 sufficient energy to reach the saltation layer. Consequently, near-wall particle concentration exhibits
 302 a strong dependence on boundary layer thickness. Supporting this, Jin et al. (2024) showed for
 303 $\delta = 1.0 \text{ m}$ that when $\theta_* = 0.0032$ (very close to the rebound threshold), the transport flux is
 304 almost entirely carried by fluid-driven particles. Because such particles have much lower energy
 305 than splash-entrained ones, their flux decays rapidly with height. As wind velocity and boundary
 306 layer thickness increase—where a thicker boundary layer at the same wind velocity corresponds to
 307 a larger argin above the rebound threshold—the decay rate of particle flux with height decreases
 308 progressively.

309 As wind velocity approaches the rebound threshold, the height of particle saltation decreases.
 310 To illustrate how particle distributions vary with wind velocity and boundary layer thickness, Fig. 6
 311 shows instantaneous particle fields at a representative moment after the aeolian sand flow has
 312 reached a steady state for $\delta = 1.0 \text{ m}$ ($\theta_* = 0.0032, 0.0043$), $\delta = 5.0 \text{ m}$ ($\theta_* = 0.0032$), and
 313 $\delta = 10.0 \text{ m}$ ($\theta_* = 0.0032$). Particle colors denote velocity, and each plotted particle represents 50
 314 actual particles. For $\delta = 1.0 \text{ m}$ at $\theta_* = 0.0032$, the maximum saltation height is about 0.03 m



(roughly 150 particle diameters), indicating weak sand transport (Fig. 6(a)). Particle motion is confined to creep or short saltation near the wall, with particle detachment relying primarily on turbulent fluctuations rather than interparticle collisions. As wind velocity increases ($\theta_* = 0.0043$, Fig. 6(b)), particle motion intensifies, velocities rise, and the aeolian sand flow develops more rapidly with increasing boundary layer thickness. Under $\delta = 10.0 \text{ m}$, the maximum saltation height approaches 0.2 m . Statistical results confirm that at higher wind velocities, increases in flux are dominated by higher particle concentrations (Fig. 5).



322

323 Fig. 6. Instantaneous particle fields for different boundary layer thicknesses
 324 ($\delta = 1.0, 5.0, 10.0 \text{ m}$) and wind velocities: (a) $\theta_* = 0.0032$, $\delta = 1.0 \text{ m}$; (b) $\theta_* = 0.0043$,
 325 $\delta = 1.0 \text{ m}$; (c) $\theta_* = 0.0032$, $\delta = 5.0 \text{ m}$; (d) $\theta_* = 0.0032$, $\delta = 10.0 \text{ m}$, where data for
 326 $\delta = 1.0 \text{ m}$ come from Jin et al. (2024).

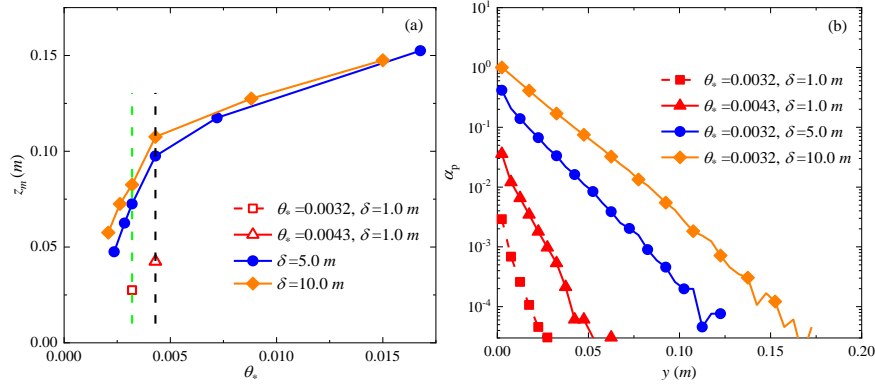
327

328 The saltation layer height z_m was also extracted (Fig. 7(a)), defined as the elevation below
 329 which 99.5% of the total mass flux occurs (Dupont et al., 2013). At wind velocities of $\theta_* = 0.0032$
 330 and 0.0043 , the saltation layer thickness for $\delta = 10.0 \text{ m}$ is approximately 3.0 and 2.5 times
 331 greater than for $\delta = 1.0 \text{ m}$, respectively. As wind velocity increases further, the differences among
 332 boundary layer thicknesses diminish, especially for $\delta = 5.0 \text{ m}$ and $\delta = 10.0 \text{ m}$.

333 To quantify the spatial intermittency of particle distributions, we define the particle spatial
 334 occupancy (α_p) as the ratio of grid cells containing particles to the total number of grid cells. Using
 335 the instantaneous particle fields shown in Fig. 6, Fig. 7(b) presents the vertical variation of α_p
 336 under different conditions. The results show that α_p decays exponentially with increasing height,
 337 reflecting its close relationship to the vertical distribution of particle volume fraction. Near the wall,
 338 α_p for $\delta = 10.0 \text{ m}$ approaches 1, indicating nearly complete grid-cell occupancy. Under the
 339 same wind velocity, α_p for $\delta = 5.0 \text{ m}$ decreases to ~ 0.4 , indicating spatial heterogeneity in

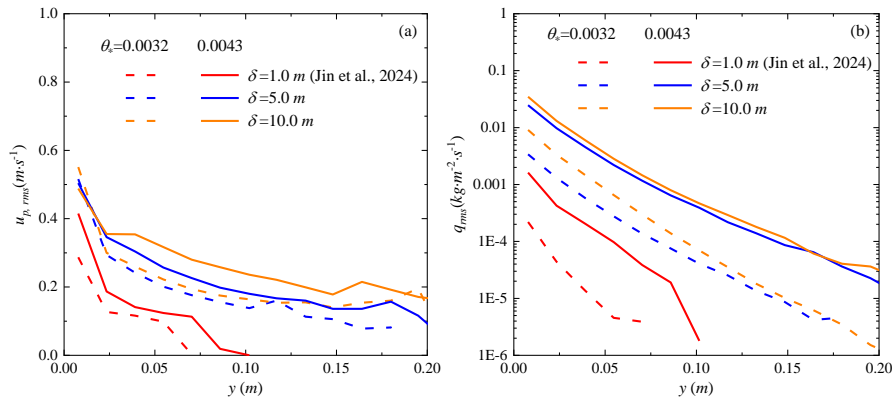


340 particle distribution, while for $\delta = 1.0 \text{ m}$, α_p falls sharply to 0.003, signifying strong spatial
 341 intermittency with particles confined to localized regions of the flow.



342
 343 Fig. 7. (a) Saltation layer height and (b) particle spatial occupancy for different boundary layer
 344 thicknesses ($\delta = 5.0, 10.0 \text{ m}$) and wind velocities.

345
 346 Increasing boundary layer thickness markedly enhances energy transfer between the turbulent
 347 flow and the particle phase. Large-scale vortices in thicker boundary layers carry greater energy and
 348 persist longer, which promotes more effective and sustained particle lifting, resulting in both vertical
 349 and horizontal dispersion and thus a more uniform distribution and significantly higher α_p values.
 350 Moreover, the effect of boundary layer thickness on α_p increases with increasing height above the
 351 wall (Fig. 7(b)).



352
 353 Fig. 8. Vertical profiles of (a) particle velocity and (b) mass flux fluctuations for different
 354 boundary layer thicknesses ($\delta = 5.0, 10.0 \text{ m}$).

355
 356 Fig. 8 presents the vertical profiles of particle velocity and mass flux fluctuations. Even when
 357 the boundary layer thickness increases to 5.0 m and 10.0 m , the peak of particle velocity



fluctuations remains located in the near-wall region. This near-wall concentration of fluctuations can markedly intensify wind erosion under low wind velocity conditions. It also reinforces the prevalence of the intermittent transport regime, dominated by fluid-driven entrainment, which differs from the continuous saltation dominated by splash-driven entrainment, where the velocity fluctuation peak typically occurs several centimeters above the bed (Feng and Wang, 2023). Across all simulated wind velocities, increasing the boundary layer thickness from 1.0 m to 5.0 m significantly amplifies the near-wall velocity fluctuation peak. However, further increases to 10.0 m produces little additional change, suggesting a gradual transition toward splash-driven entrainment. Differences in velocity fluctuations associated with boundary layer thickness become more apparent only at higher elevations above the wall.

Near-threshold sediment transport rate fluctuations also differ from those in continuous transport. As boundary layer thickness increases, the magnitude of transport rate fluctuations rises but the incremental effect diminishes, particularly at higher wind velocities. Consequently, the influence of boundary layer thickness on mass flux fluctuations weakens as wind velocity increases. This behavior mirrors the response of the mean sediment transport rate, reflecting the fact that as wind velocity approaches the splash-driven entrainment threshold, both fluid- and splash-driven processes become less sensitive to variations in boundary layer thickness.

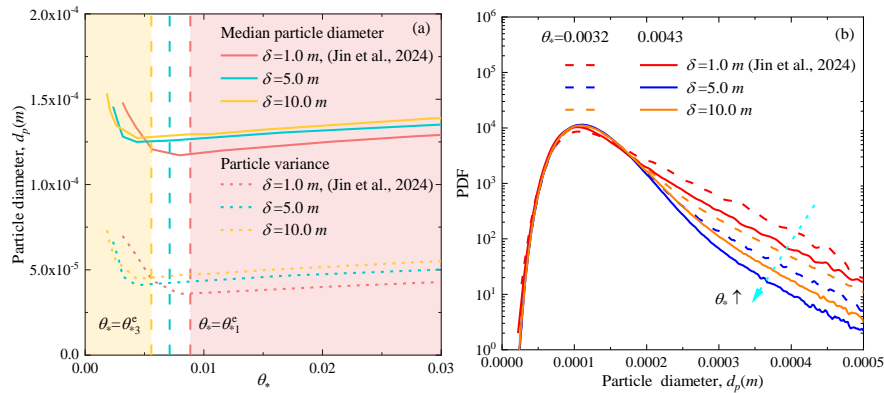


Fig. 9 (a) Mean and variance, and (b) probability density distribution of particle diameter for different boundary layer thicknesses ($\delta = 5.0, 10.0$ m) as a function of wind velocity.

Under conditions with boundary layer thicknesses $\delta = 5.0, 10.0$ m (Fig. 9(a)), the variation of particle diameter parameters reveals two distinct regimes. When wind velocity is below the impact entrainment threshold (θ_*^c), both the mean and variance of airborne particle diameter decrease with increasing θ_* . In contrast, once wind velocity exceeds θ_*^c , both parameters become proportional to θ_* , consistent with the conclusions drawn for $\delta = 1.0$ m and supporting the



validity of defining the critical threshold based on transport rate. At lower wind velocities, the relationship between mean and variance differs across boundary layer thicknesses: $d_{p,ave,\delta=1.0\text{ m}} / (d_{p,var,\delta=1.0\text{ m}}) > d_{p,ave,\delta=5.0\text{ m}} / (d_{p,var,\delta=5.0\text{ m}}) > d_{p,ave,\delta=10.0\text{ m}} / (d_{p,var,\delta=10.0\text{ m}})$. Conversely, thicker boundary layer thicknesses result in greater mean and variance. Simulation results show that the critical Shields numbers for $\delta=10.0\text{ m} > \delta=5.0\text{ m}$, and $\delta=5.0, 10\text{ m} > \delta=1.0\text{ m}$ are $\theta_{*1} = 0.003$ and $\theta_{*2} = 0.005$, respectively. For wind velocities of $\theta_* = 0.0032$ and 0.0043 , lying between these two critical values, the relationship between mean and variance shifts accordingly: $d_{p,ave,\delta=1.0\text{ m}} / (d_{p,var,\delta=1.0\text{ m}}) > d_{p,ave,\delta=10.0\text{ m}} / (d_{p,var,\delta=10.0\text{ m}}) > d_{p,ave,\delta=5.0\text{ m}} / (d_{p,var,\delta=5.0\text{ m}})$, as also confirmed by the probability density distributions in Fig. 9(b).

As wind velocity increases (θ_* rising from 0.0032 to 0.0043), the probability of entraining larger particles decreases because both $\theta_* = 0.0032$ and 0.0043 remain below θ_*^c , meaning that fluid-driven entrainment still dominates particle transport. Under these conditions, the enhanced near-wall transport flux induces a reduction in local wind velocities due to particle loading (Jin et al., 2021), which further suppresses the fluid entrainment of larger particles.

4. Discussion and Conclusions

This study investigates the role of boundary layer thickness in modulating near-threshold aeolian sediment transport, a process characterized by high intermittency. Recognizing that traditional models, often assuming steady, continuous sediment transport governed by a single threshold (Kawamura, 1951; White, 1979; Creyssels et al., 2009), fail to capture near-threshold behavior, this research addresses a critical knowledge gap. The primary objective is to systematically elucidate how different boundary layer conditions influence the turbulent flow field and the resulting particle entrainment and transport mechanisms near threshold. To achieve this, the study employs the three-dimensional large-eddy simulation coupled with a Lagrangian saltation model, aiming to provide a mechanistic understanding of wind tunnel-field discrepancies.

Increasing boundary layer thickness enhances extreme values in wall-shear stress fluctuations. As a result, both the impact entrainment threshold (θ_*^c or u_*^c) and the rebound threshold (θ_*^r or u_*^r) decrease. For thick boundary layers ($\delta = 5.0\text{ m}$ and 10.0 m), the rebound threshold wind velocity can drop below 50% of values typically observed in conventional wind tunnel experiments. Sediment transport responds differentially to wind velocity: at very low wind velocities ($\theta_* < \theta_*$), transport increases markedly with thickness under fluid-driven entrainment; at high wind velocities ($\theta_* > 21\theta_{*2}^c$ or $> 27\theta_{*3}^c$), it scales proportionally with thickness under splash-driven entrainment; and at intermediate wind velocities, the effect is negligible. Near-bed particle velocity, concentration, saltation height, and airborne particle diameter all increase with boundary layer



418 thickness, accompanied by reduced intermittency and more uniform spatial distributions.

419 A thicker boundary layer accommodates a broader range of turbulent scales, fostering stronger,
 420 large-scale coherent structures that generate more extreme instantaneous stress events (Pähtz et al.,
 421 2018). This enhanced turbulence facilitates particle entrainment at lower mean wind velocities,
 422 which also explains why the rebound threshold can be less than half the typical wind-tunnel value
 423 (Rasmussen and Sørensen, 1999). Notably, the impact entrainment threshold exhibits a more
 424 pronounced reduction, implying that sustaining continuous transport becomes feasible at relatively
 425 lower velocities as boundary layer thickness increases. Furthermore, the dependence of sand
 426 transport on boundary layer thickness reveals distinct regimes: at low winds, enhanced turbulent
 427 fluctuations directly loft more particles, while at high winds, the system transitions to a splash-
 428 dominated regime where transport capacity scales with the thicker boundary layer (Feng and Wang,
 429 2023).

430 Thicker boundary layers promote more energetic large-scale turbulent structures that
 431 effectively lift and disperse particles, leading to a more uniform distribution and reduced
 432 intermittency. This mechanism explains previous field observations of longer and more persistent
 433 "streamers" (Baas and Sherman, 2005; Sherman et al., 2013). Unlike the findings of Feng and Wang
 434 (2023), which showed increased concentration only away from the wall, our results reveal the
 435 unique nature of the near-threshold, fluid-entrainment-dominated regime. The observed reversal in
 436 particle size trend is due to the shift from fluid-driven to splash-driven entrainment.

437 Although this study reveals the significant influence of boundary layer thickness on near-
 438 threshold aeolian sediment transport, several issues require further investigation in the future. This
 439 study examined only three boundary layer thicknesses and a single particle size range. Future work
 440 should extend to thicker boundary layers (closer to realistic atmospheric conditions) and broader
 441 particle size distributions to clarify the underlying mechanisms systematically. The current model
 442 does not account for multiphysical processes, such as interparticle collisions, electrostatic
 443 interactions, or humidity effects, which significantly influence the entrainment and transport of fine
 444 particles in natural environments.

445 Our findings fundamentally shift how the atmospheric boundary layer should be viewed in dust
 446 emission modeling. By demonstrating that thicker boundary layers can halve the entrainment
 447 thresholds and alter particle size distributions, we provide the mechanistic basis for the known
 448 discrepancy between wind-tunnel models and field observations. This implies that current climate
 449 models likely underestimate dust emissions. Integrating boundary layer thickness into dust emission
 450 schemes is therefore critical for accurate simulation of aerosol radiative forcing, cloud processes,
 451 and the evolution of arid landscapes in a changing climate.



452
 453 *Data availability.* The data that support the findings of this study are available in the Figshare
 454 repository (<https://doi.org/10.6084/m9.figshare.30245776>). Additional data related to this paper and
 455 the codes may be requested from the authors.
 456
 457 *Author contributions.* Lifeng Zhou designed and organized the research and its approach. Ting Jin
 458 carried out the simulation, analyzed the results, wrote the manuscript and carefully modified the
 459 manuscript. All authors contributed to the paper.
 460
 461 *Competing interests.* The authors declare that they have no conflict of interest.
 462
 463 *Acknowledgements.* This work was funded by the National Natural Science Foundation of China
 464 (No. 12202170) and the Yunnan Fundamental Research Projects (No. 202301AT070164).
 465
 466 **References**
 467 Almeida, M. P., Andrade, J. S., Herrmann, H. J., 2006, Aeolian transport layer, *Physical Review Letters*,
 468 96(1), 018001.
 469 Anderson, R. S., Haff, P. K., 1991, Wind modification and bed response during saltation of sand in air,
 470 *Acta Mechanica Supplementum*, 1, 21-51.
 471 Baas, A. C. W., Sherman, D. J., 2005, Formation and behavior of aeolian streamers, *Journal of*
 472 *Geophysical Research: Atmospheres*, 110(F3), F03011.
 473 Baas, A. C. W., Sherman, D. J., 2006, Spatiotemporal variability of aeolian sand transport in a coastal
 474 dune environment, *Journal of Coastal Research*, 22(5), 1198-1205.
 475 Bagnold, R. A., 1941, *The physics of blown sand and desert dunes*, Springer Netherlands.
 476 Balakumar, B. J., Adrian, R. J., 2007, Large- and very-large-scale motions in channel and boundary-layer
 477 flows, *Philos Trans A Math Phys Eng*, 365(1852), 665-681.
 478 Butterfield, G. R., 1998, Transitional behaviour of saltation: wind tunnel observations of unsteady winds,
 479 *Journal of Arid Environments*, 39(3), 377-394.
 480 Carneiro, M. V., Rasmussen, K. R., Herrmann, H. J., 2015, Bursts in discontinuous Aeolian saltation,
 481 *Scientific Reports*, 5(1), 1-8.
 482 Clift, R., Grace, J. R., Weber, M. E., 1978, *Bubbles, Drops and Particles*, New York: Academic.
 483 Clifton, A., Rüedi, J. D., Lehning, M., 2006, Snow saltation threshold measurements in a drifting-snow
 484 wind tunnel, *Journal of Glaciology*, 52(179), 585-596.
 485 Creyssels, M., Dupont, P., Ould El Moctar, A., Valance, A., Cantat, I., Jenkins, J. T., Pasini, J. M.,
 486 Rasmussen, K. R., 2009, Saltating particles in a turbulent boundary layer: experiment and theory, *Journal*
 487 *of Fluid Mechanics*, 625, 47-74.
 488 Dong, Z., Liu, X., Wang, H., Wang, X., 2003, Aeolian sand transport: a wind tunnel model, *Sedimentary*
 489 *Geology*, 161(1), 71-83.
 490 Dun, H. C., Huang, N., 2020, Dust emission in farmland caused by aerodynamic entrainment and surface
 491 renewal, *Atmos. Chem. Phys.*, 1-12.



- 492 Dupont, S., Bergametti, G., Marticorena, B., Simoëns, S., 2013, Modeling saltation intermittency, *Journal*
493 *of Geophysical Research: Atmospheres*, 118(13), 7109-7128.
- 494 Ellis, J. T., Sherman, D. J., Farrell, E. J., Li, B., 2012, Temporal and spatial variability of aeolian sand
495 transport: Implications for field measurements, *Aeolian Research*, 3(4), 379-387.
- 496 Feng, S. J., Wang, P., 2023, The influences of boundary layer thickness on the characteristics of saltation
497 sand flow—A large eddy simulation study, *Aeolian Research*, 60, 100853.
- 498 Guala, M., Hommema, S. E., Adrian, R. J., 2006, Large-scale and very-large-scale motions in turbulent
499 pipe flow, *Journal of Fluid Mechanics*, 554, 521-542.
- 500 Huang, N., He, P. L., Zhang, J., 2020, Large-eddy simulation of sand transport under unsteady wind,
501 *Geomorphology*, 358, 107105.
- 502 Jia, S. M., Wang, Z. S., 2021, Simulation of aerodynamic entrainment with inter-particle cohesions based
503 on discrete element method, *Earth Surface Processes and Landforms*, 46(7), 1410-1418.
- 504 Jin, T., Chen, Z. Z., Wang, P., 2023, Performance assessment of wall-modeled large-eddy simulation for
505 modeling aeolian two-phase flow, *European Journal of Mechanics / B Fluids*, 100, 291-301.
- 506 Jin, T., Wang, P., Cao, B., 2024, Transport characteristics of aeolian sand near different thresholds, *Catena*,
507 247, 108541.
- 508 Jin, T., Wang, P., Zheng, X. J., 2021, Characterization of Wind-blown Sand with Near-wall Motions and
509 Turbulence: from Grain-scale Distributions to Sediment Transport, *Journal of Geophysical Research:*
510 *Earth Surface*, 126(8).
- 511 Kawamura, R., 1951, Study of sand movement by wind, *Institute of Science and Technology*, 5(3), 95-
512 112.
- 513 Kim, K., Baek, S. J., Sung, H. J., 2002, An implicit velocity decoupling procedure for the incompressible
514 Navier-Stokes equations, *International Journal for Numerical Methods in Fluids*, 38(2), 125-138.
- 515 Kok, J. F., 2010a, Difference in the Wind Speeds Required for Initiation versus Continuation of Sand
516 Transport on Mars: Implications for Dunes and Dust Storms, *Physical Review Letters*, 104(7), 074502.
- 517 Kok, J. F., 2010b, An improved parameterization of wind-blown sand flux on Mars that includes the
518 effect of hysteresis, *Geophysical Research Letters*, 37(12), 986-992.
- 519 Kok, J. F., Renno, N. O., 2009, A comprehensive numerical model of steady state saltation (COMSALT),
520 *Journal of Geophysical Research*, 114(D17), D17204.
- 521 Leenders, J. K., Boxel, J. H., Sterk, G., 2005, Wind forces and related saltation transport, *Geomorphology*,
522 71, 357-372.
- 523 Li, S. H., Li, C., Yao, D., Ge, X. D., Zhang, G. P., 2020, Wind tunnel experiments for dynamic modeling
524 and analysis of motion trajectories of wind-blown sands, *The European Physical Journal E*, 43(4), 22.
- 525 Liu, H. Y., Feng, Y. E., Zheng, X. J., 2022, Experimental investigation of the effects of particle near-wall
526 motions on turbulence statistics in particle-laden flows, *Journal of Fluid Mechanics*, 943, A8.
- 527 Liu, H. Y., Shi, Y. X., Zheng, X. J., 2021, Evolution of turbulent kinetic energy during the entire
528 sandstorm process, *Atmos. Chem. Phys.*, 22(13), 8787-8803.
- 529 Lu, H., Raupach, M. R., Richards, K. S., 2005, Modeling entrainment of sedimentary particles by wind
530 and water: A generalized approach, *Journal of Geophysical Research: Atmospheres*, 110(D24).
- 531 Martin, R. L., Kok, J. F., 2018, Distinct thresholds for the initiation and cessation of aeolian saltation
532 from field measurements, *Journal of Geophysical Research: Earth Surface*, 123(7), 1546-1565.
- 533 Marusic, I., Baars, W. J., Hutchins, N., 2017, Scaling of the streamwise turbulence intensity in the context
534 of inner-outer interactions in wall turbulence, *Physical Review Fluids*, 2(10), 100502.
- 535 Marusic, I., McKeon, B. J., Monkewitz, P. A., Nagib, H. M., Smits, A. J., Sreenivasan, K. R., 2010, Wall-



536 bounded turbulent flows at high Reynolds numbers: Recent advances and key issues, *Physics of Fluids*,
 537 22(6), 065103.

538 Mathis, R., Hutchins, N., Marusic, I., 2009, Large-scale amplitude modulation of the small-scale
 539 structures in turbulent boundary layers, *Journal of Fluid Mechanics*, 628, 311-337.

540 Pähtz, T., Valyrakis, M., Zhao, X. H., Li, Z. S., 2018, The critical role of the boundary layer thickness
 541 for the initiation of aeolian sediment transport, *Geosciences*, 8(9), 314.

542 Parajuli, S. P., Zobeck, T. M., Kocurek, G., Yang, Z. L., Stenchikov, G. L., 2016, New insights into the
 543 wind - dust relationship in sandblasting and direct aerodynamic entrainment from wind tunnel
 544 experiments, *Journal of Geophysical Research: Atmospheres*, 121(4), 1776-1792.

545 Porté-Agel, F., Meneveau, C., Parlange, M. B., 2000, A scale-dependent dynamic model for large-eddy
 546 simulation: application to a neutral atmospheric boundary layer, *Journal of Fluid Mechanics*, 415, 261-
 547 284.

548 Rasmussen, K. R., Sørensen, M., 1999, Aeolian mass transport near the saltation threshold, *Earth Surface
 549 Processes and Landforms*, 24(5), 413-422.

550 Schlatter, P., Örlü, R., 2010, Assessment of direct numerical simulation data of turbulent boundary layers,
 551 *Journal of Fluid Mechanics*, 659, 116-126.

552 Serafimovich, A., Thomas, C., Foken, T., 2011, Vertical and Horizontal Transport of Energy and Matter
 553 by Coherent Motions in a Tall Spruce Canopy, *Boundary-Layer Meteorology*, 140(3), 429-451.

554 Shao, Y. P. (2008), *Physics and modelling of wind erosion*, Heidelberg: Springer.

555 Shao, Y. P., Li, A., 1999, Numerical modelling of saltation in the atmospheric surface layer, *Boundary-
 556 Layer Meteorology*, 91(2), 199-225.

557 Sherman, D. J., Houser, C., Ellis, J. T., Farrell, E. J., Li, B. L., Davidson-Arnott, R. G. D., Baas, A. C.
 558 W., Maia, L. P., 2013, Characterization of aeolian streamers using time-average videography, *Journal of
 559 Coastal Research*, 165, 1331-1336.

560 Sherman, D. J., Jackson, D., Namikas, S. L., Wang, J., 1998, Wind-blown sand on beaches: an evaluation
 561 of models, *Geomorphology*, 22, 113-133.

562 Spies, P. J., McEwan, I. K., Butterfield, G. R., 2000, One-dimensional transitional behaviour in saltation,
 563 *Earth Surface Processes and Landforms*, 25(5), 505-518.

564 Stout, J. E., Zobeck, T. M., 1997, Intermittent saltation, *Sedimentology*, 44(5), 959-970.

565 Wang, P., Feng, S. J., Zheng, X. J., Sung, H. J., 2019, The scale characteristics and formation mechanism
 566 of aeolian sand streamers based on large eddy simulation, *Journal of Geophysical Research: Atmospheres*,
 567 124(21), 11372-11388.

568 Wang, P., Zheng, X. J., 2014, Saltation transport rate in unsteady wind variations, *European Physical
 569 Journal E*, 37(5), 1-11.

570 Wang, Z. T., Zhang, C. L., Wang, H. T., 2014, Intermittency of aeolian saltation, *European Physical
 571 Journal E*, 37(12), 1-6.

572 White, B. R., 1979, Soil transport by winds on mars, *Journal of Geophysical Research*, 84(B9), 4643-
 573 4651.

574 Yang, X., Sadique, J., Mittal, R., Meneveau, C., 2015, Integral wall model for large eddy simulations of
 575 wall-bounded turbulent flows, *Physics of Fluids*, 27(2), 025112.

576 Zhang, J., Li, G., Shi, L., Huang, N., Shao, Y. P., 2022, Impact of turbulence on aeolian particle
 577 entrainment: results from wind-tunnel experiments, *Atmos. Chem. Phys.*, 22(14), 9525-9535.

578 Zheng, X. J., Jin, T., Wang, P., 2020, The influence of surface stress fluctuation on saltation sand transport
 579 around threshold, *Journal of Geophysical Research: Earth Surface*, 125(5), e2019JF005246.



580 Zhou, Y. H., Guo, X., Zheng, X. J., 2002, Experimental measurement of wind-sand flux and sand
581 transport for naturally mixed sands, *Physical Review E*, 66, 021305.
582 Zhu, H. Y., Pan, C., Wang, J. J., Liang, Y. R., Ji, X. C., 2019, Sand-turbulence interaction in a high-
583 reynolds-number turbulent boundary layer under net sedimentation conditions, *International Journal of*
584 *Multiphase Flow*, 119(1), 56-71.